Instrument Science Report WFC3 2009-38

WFC3 SMOV Programs 11436/8: UVIS On-orbit PSF Evaluation

G. F. Hartig
10 November 2009

ABSTRACT

We have assessed the image quality of the WFC3 UVIS channel on orbit, following its alignment to the HST OTA. Point spread function measurements of ~100 stars over the field were made in the UV (F275W) and red (F621M) and compared to model computations and CEI specifications. Deep, core-saturated images of a standard star, sampling the field at 5 locations, were also obtained to evaluate the PSF wings. All encircled energy specifications are met or exceeded, as expected from previous ground testing and modeling results. The optical model has been correlated to the observed PSF properties and may be used to predict performance over the full UVIS spectral range.

Introduction

We have previously discussed measurements of the UVIS PSF over the field, through four filters spanning the spectral range, in thermal-vacuum tests with the instrument in its final flight configuration (Hartig 2008a). The image quality and wavefront error (Hartig 2008b) were generally found to be excellent, but modeling was required to extend the ground measurements with the CASTLE stimulus to the on-orbit configuration with the HST OTA.

Following alignment of the UVIS channel to the OTA (involving adjustment of the corrector mechanism to bring the images into focus and optimize the pupil alignment, thereby minimizing the coma that results from pupil shear), a set of confirmatory images were obtained during the SMOV4 campaign to evaluate the optical performance and verify that specifications were achieved.

Observations

The PSF evaluation data were obtained with two SMOV4 programs, 11436 and 11438, executed on 1 Aug and 30 Jul 2009, respectively. Tables 1 and 2 present the observation details. The UVIS detector was operated at its nominal temperature, –83C, and nominal gain (1.5 e^-/DN). The target for proposal 11436 is a field in NGC-188, an old astrometric open cluster, chosen to yield a reasonable density of appropriately bright stars to permit accurate encircled energy measurements while sampling the FOV well with relatively short

exposures in both filters. The program 11438 target is GD-153, a photometric standard DA white dwarf, selected for its isolation and brightness, which allow measurement of the PSF wings in reasonable exposures without complications from nearby sources.

Table 1. Prog 11436 UVIS PSF Evaluation Observation Log

rootname	imsize	filter	obs_date	obs_time	exptime	pos-targ
iab701011	FullFrame	F621M	8/01/2009	19:20:06	60	(0,20)
iab701021	FullFrame	F621M	8/01/2009	19:36:40	60	(0,0)
iab701031	FullFrame	F275W	8/01/2009	19:42:31	1360	(0,0)
iab701041	FullFrame	F621M	8/01/2009	20:46:04	60	(20,0)
iab701051	FullFrame	F621M	8/01/2009	21:02:38	60	(20,20)
iab701061	FullFrame	F275W	8/01/2009	21:08:29	1360	(20,20)
iab701071	FullFrame	F275W	8/01/2009	22:21:49	1280	(20,0)
iab701081	FullFrame	F275W	8/01/2009	22:47:25	1280	(0,20)

POS-TARG offsets were employed to improve field coverage, to avoid blemishes and to ameliorate potential persistence effects in the highly-saturated exposures used to investigate the PSF wings. No persistence has been previously detected (Hartig and Baggett, 2004), nor is any seen in these images. Each image was CR-split into pairs of exposures for cosmic ray rejection. Subarrays were used for the shorter exposures of 11438, to sample the PSF core region with exposure depth increasing from about half full-well to about 40 times full-well, while highly saturated full-frame images were obtained to study the far wings and investigate possible ghosting, stray light, and electronic cross-talk anomalies. Five pointings, toward each corner of the field and near field center, were used for program 11438.

Table 2. Prog 11438 UVIS PSF Wing Evaluation Observation Log

rootname	readamp	imsize	filter	obs_date	obs_time	exptime	pos-targ
iabk02011	C	400x400	F275W	7/30/2009	9:36:35	10	(-50.7,-54.9)
iabk02021	C	400x400	F275W	7/30/2009	9:38:23	20	(-50.7,-54.9)
iabk02031	C	400x400	F275W	7/30/2009	9:40:21	50	(-50.7,-54.9)
iabk02041	C	400x400	F275W	7/30/2009	9:42:49	200	(-50.7,-54.9)
iabk02051	ABCD	FullFrame	F275W	7/30/2009	9:47:45	800	(-50.7,-54.9)
iabk02061	C	400x400	F625W	7/30/2009	10:05:46	10	(-50.2,-54.4)
iabk02071	C	400x400	F625W	7/30/2009	10:07:34	20	(-50.2,-54.4)
iabk02081	C	400x400	F625W	7/30/2009	10:09:32	50	(-50.2,-54.4)
iabk02091	C	400x400	F625W	7/30/2009	10:12:00	200	(-50.2,-54.4)
iabk020a1	ABCD	FullFrame	F625W	7/30/2009	11:03:55	800	(-50.2,-54.4)
iabk020b1	A	400x400	F625W	7/30/2009	11:21:33	10	(-50.7, 48.0)
iabk020c1	A	400x400	F625W	7/30/2009	11:23:21	20	(-50.7, 48.0)
iabk020d1	A	400x400	F625W	7/30/2009	11:25:19	50	(-50.7, 48.0)
iabk020e1	A	400x400	F625W	7/30/2009	11:27:47	200	(-50.7, 48.0)
iabk020f1	ABCD	FullFrame	F625W	7/30/2009	11:32:43	800	(-50.7, 48.0)
iabk020g1	A	400x400	F275W	7/30/2009	12:44:36	10	(-50.2, 47.5)
iabk020h1	A	400x400	F275W	7/30/2009	12:46:24	20	(-50.2, 47.5)
iabk020i1	A	400x400	F275W	7/30/2009	12:48:22	50	(-50.2, 47.5)
iabk020j1	A	400x400	F275W	7/30/2009	12:50:50	200	(-50.2, 47.5)
iabk020k1	ABCD	FullFrame	F275W	7/30/2009	12:55:46	800	(-50.2, 47.5)
iabk03011	D	400x400	F625W	7/30/2009	11:08:53	10	(50.7,-48.0)
iabk03021	D	400x400	F625W	7/30/2009	11:10:41	20	(50.7,-48.0)

iabk03031	D	400x400	F625W	7/30/2009	11:12:39	50	(50.7,-48.0)
iabk03041	D	400x400	F625W	7/30/2009	11:15:07	200	(50.7,-48.0)
iabk03051	ABCD	FullFrame	F625W	7/30/2009	11:20:03	800	(50.7,-48.0)
iabk03061	D	400x400	F275W	7/30/2009	11:38:04	10	(50.2,-47.5)
iabk03071	D	400x400	F275W	7/30/2009	11:39:52	20	(50.2,-47.5)
iabk03081	D	400x400	F275W	7/30/2009	11:41:50	50	(50.2,-47.5)
iabk03091	D	400x400	F275W	7/30/2009	11:44:18	200	(50.2,-47.5)
iabk030a1	ABCD	FullFrame	F275W	7/30/2009	12:39:56	800	(50.2,-47.5)
iabk04011	B	400x400	F275W	7/30/2009	14:33:32	10	(50.7, 54.9)
iabk04021	B	400x400	F275W	7/30/2009	14:35:20	20	(50.7, 54.9)
iabk04031	B	400x400	F275W	7/30/2009	14:37:18	50	(50.7, 54.9)
iabk04041	B	400x400	F275W	7/30/2009	14:39:46	200	(50.7, 54.9)
iabk04051	ABCD	FullFrame	F275W	7/30/2009	14:44:42	800	(50.7, 54.9)
iabk04061	B	400x400	F625W	7/30/2009	15:57:36	10	(50.2, 54.4)
iabk04071	B	400x400	F625W	7/30/2009	15:59:24	20	(50.2, 54.4)
iabk04081	B	400x400	F625W	7/30/2009	16:01:22	50	(50.2, 54.4)
iabk04091	B	400x400	F625W	7/30/2009	16:03:50	200	(50.2, 54.4)
iabk040a1	ABCD	FullFrame	F625W	7/30/2009	16:08:46	800	(50.2, 54.4)
iabk05011	A	400x400	F625W	7/30/2009	1:30:58	10	(0.0, 0.0)
iabk05021	A	400x400	F625W	7/30/2009	1:32:50	20	(0.0, 0.0)
iabk05031	A	400x400	F625W	7/30/2009	1:34:52	50	(0.0, 0.0)
iabk05041	A	400x400	F625W	7/30/2009	1:37:24	200	(0.0, 0.0)
iabk05051	ABCD	FullFrame	F625W	7/30/2009	1:42:24	800	(0.0, 0.0)
iabk05061	B	400x400	F275W	7/30/2009	2:00:25	10	(0.5, 0.5)
iabk05071	B	400x400	F275W	7/30/2009	2:02:19	20	(0.5, 0.5)
iabk05081	B	400x400	F275W	7/30/2009	2:04:23	50	(0.5, 0.5)
iabk05091	B	400x400	F275W	7/30/2009	2:06:57	200	(0.5, 0.5)
iabk050a1	ABCD	FullFrame	F275W	7/30/2009	2:55:43	800	(0.5, 0.5)

Analyses

The NGC-188 field images (11436) were analyzed by first identifying suitable stars, which are of sufficient signal level (>3-5 kDN in the peak px), and isolated from neighbors and field edges, bad pixels, etc. in order to permit accurate encircled energy computation. This selection was accomplished with IDL tool *find_psfs*, which, after automatically selecting suitable PSFs, permits manual inspection of the results, enabling further vetting. The POS-TARG offset fields were independently treated, with results from all fields collated for analysis and plotting.

Measurements of each PSF were made using *wfc3_psf_eval*, which computes the encircled energy (EE) within specified apertures, the FWHM of the best fit 2-D Gaussian (in px), peak pixel fraction, sharpness (sum of the square of the unity-normalized PSF) and ellipticity. Because an aperture of ~1 arcsec radius is used for the computations, the EE and peak fraction values are corrected for the PSF flux outside that aperture, amounting to ~7% and 5% for the F275W and F621M images, respectively, as measured using the PSF wing evaluation data (see below). The sharpness is not sensitive to the PSF wings, but is dominated by the core within a few pixels radius. The OTA breathing model was also used to estimate the telescope focus state at the time of each observation; this is useful for confirmation of the UVIS corrector focus setting.

Figure 1 displays some measurement results for each selected star at the appropriate field location. The relative core EE within the relevant CEI spec diameter (0.2 and 0.25 arcsec for 250 and 633 nm, respectively) for each filter is indicated by the color, ranging from violet (low) to red (high). Circle diameter indicates the relative sharpness (left) and FWHM (right); the same scale is used for both filters. There is little evident correlation between FWHM and EE; the former being sensitive to the centration of the PSF with respect to the pixel boundaries. The sharpness demonstrates more correlation to the EE, but is also somewhat sensitive to PSF centration.

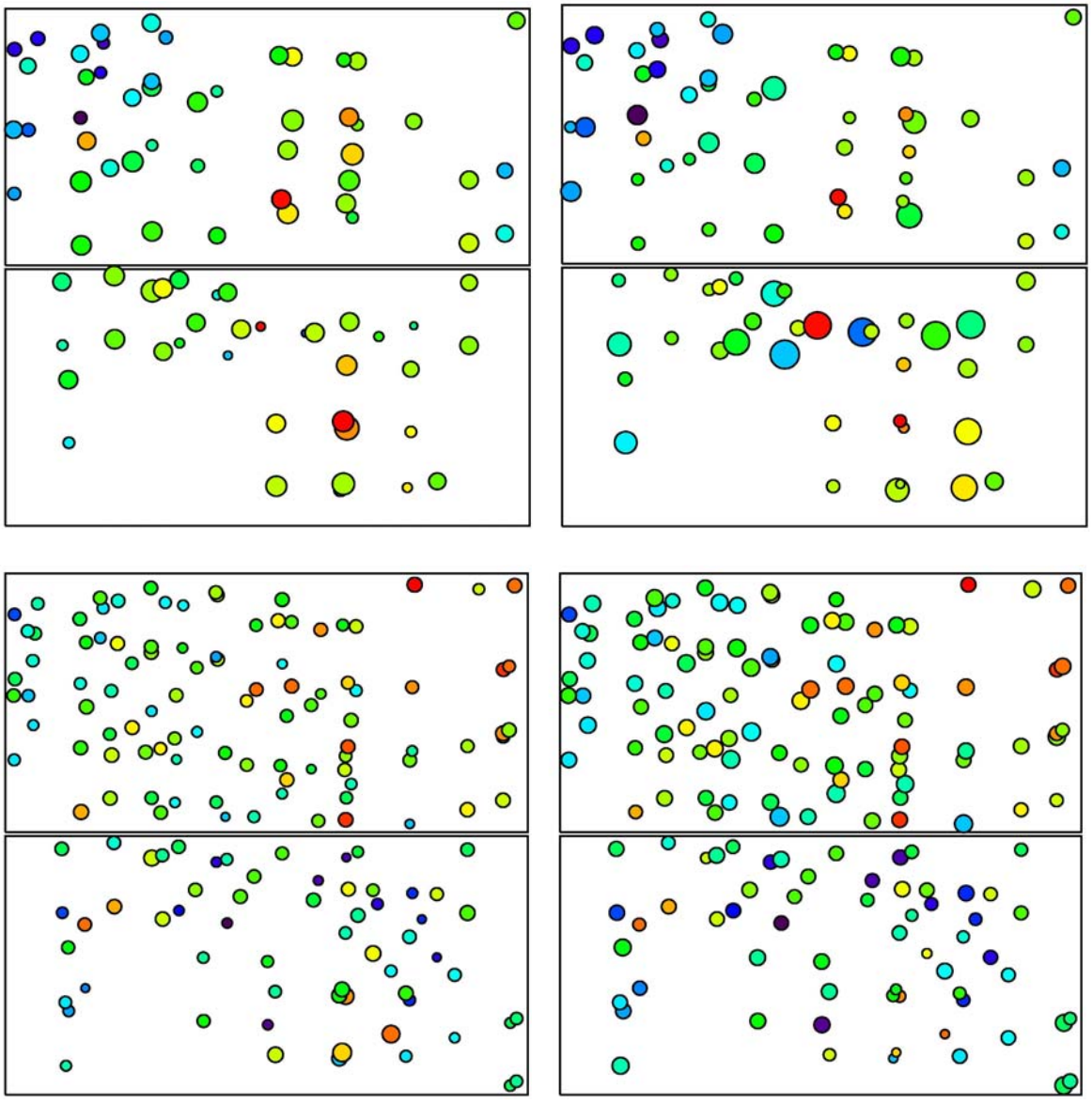

Figure 1. Measured PSF field locations and parameters for selected stars in the Program 11436 images through F275W (top) and F621M (bottom). The relative EE in the PSF core is indicated by the color of the circles, while the relative sharpness (left) and FWHM (right) are indicated by the diameter.

The PSF core measurements for the two filters are summarized in Tables 3 and 4, with their average, range and standard deviation; 86 stars were measured for F275W and 157 for

F621M. The three EE values listed in the table are for diameters of 0.15, 0.2, and 0.25 arcsec; the latter two are the CEI spec core EE diameters for 250 and 633 nm, respectively. While the core EE spec of 75% within 0.25 arcsec for 633 nm is easily achieved, the spec of 70% in 0.2 arcsec for 250 nm is exceeded by a smaller margin, as had been predicted from ground testing and modeling (Hartig, 2008a), after the decrement from the effective wavelength of the F275W to the spec wavelength is accounted for, via modeling.

Table 3. Program 11436 UVIS F275W PSF Measurement Summary

n=83	EE.15	EE.20	EE.25	shrp	peak	fwhm	ellip
avg:	0.644	0.743	0.794	0.062	0.145	1.858	0.108
min:	0.597	0.706	0.758	0.045	0.102	1.548	0.025
max:	0.680	0.773	0.830	0.077	0.194	2.326	0.198
std:	0.019	0.014	0.013	0.007	0.023	0.183	0.052

Table 4. Program 11436 UVIS F621M PSF Measurement Summary

n=157	EE.15	EE.20	EE.25	shrp	peak	fwhm	ellip
avg:	0.587	0.709	0.791	0.055	0.139	1.783	0.074
min:	0.557	0.682	0.770	0.047	0.110	1.549	0.028
max:	0.614	0.731	0.809	0.066	0.182	1.925	0.131
std:	0.012	0.011	0.008	0.003	0.014	0.066	0.027

The program 11438 data were combined to produce high dynamic range images for each filter at the five tested field points. This construction was achieved by first combining the CR-split pairs using the calwf3 pipeline, then, starting with the longest (full field) exposure, successively replacing saturated pixels and their immediate neighbors with values from the next shorter (subarray) exposure, scaled by relative exposure time, and repeating, such that only the central few pixels of the shortest exposure PSF were included. This results in images with effective peak pixel signal of ~5 Me^-, and permits evaluation of the azimuthally-averaged PSF wings out to radius >5 arcsec, for comparison with CEI specifications.

Figure 2 is a montage of the combined PSF core images, displayed at their approximate field locations, for each of the two filters with a logarithmic stretch. The images are magnified relative to the field size by a factor 10 and subtend ~4 arcsec. The asymmetric structure in the near wings is nearly field-independent, and is due largely to the OTA mirror zonal polishing errors, which transfer an increasing fraction of flux from the PSF core into the broadening wings as wavelength decreases into the UV. The measured EE within the core spec diameter is shown near each PSF; the variations are judged to be within the measurement uncertainties. However, these core EE values are slightly lower than those reported above for many more stars; this is likely due to the effects of the UVIS shutter-induced blur, since these shortest exposures (used for the PSF core in these composite images) were each 5s, while longer exposures, less susceptible to the effect were employed for program 11436.

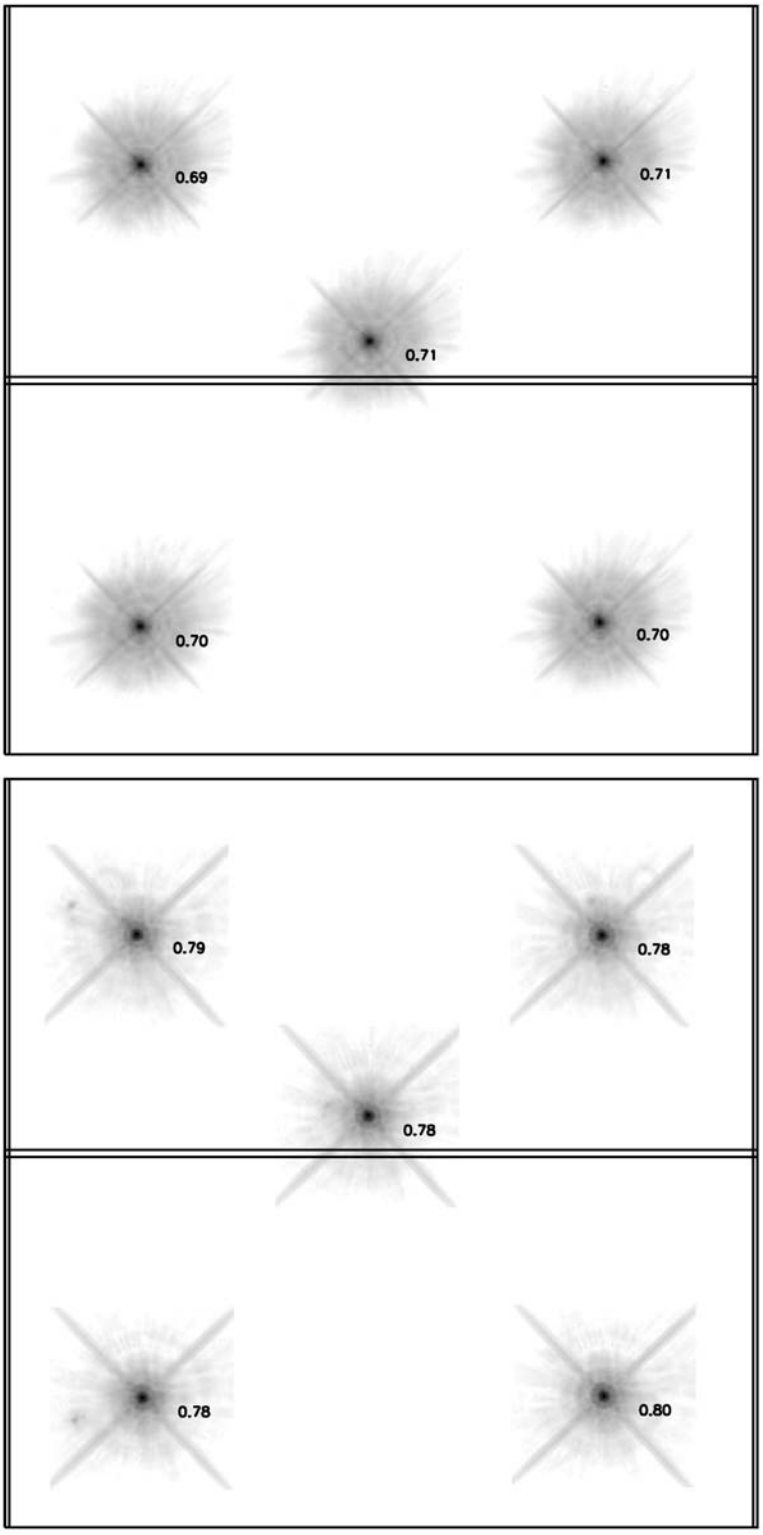

Figure 2 . Montages of measured PSF cores from Program 11438 illustrating their field position for filter F275W (top) and F625W (bottom), displayed with a log stretch. The images are magnified by a factor 10 relative to the field and are corrected for geometric distortion. Core EE values are shown.

Larger versions of the combined images, subtending ~20 arcsec, are shown in Figure 3 for two of the field locations (B amp corner for F275W, A amp for F625W). They are not corrected for geometrical distortion, so are visibly elongated along the UL-LR diagonal, due to the detector tilt with respect to the chief ray inherent in the UVIS design. Although the target was chosen to be isolated, a number of field galaxies appear in the F625W image (bottom) but are absent in the F275W image; these galaxies are also seen in the IR channel images of the same target (Hartig, 2009). Some detector artifacts, including warm pixels and imperfectly removed cosmic ray hits are also evident.

Two different types of "ghost" artifacts are visible in the images. As expected from the UVIS channel design, there are low-level ghosts due to reflections between the four surfaces of the two anti-reflection-coated detector windows: these are the sets of relatively large diameter, ring-shaped ghosts seen extending out at PA ~330º (top) and PA ~30º (bottom). Also evident is a filter ghost, due to reflections between the surfaces of the F625W filter (bottom), which appears almost point-like at a radius of 1.6 arcsec and PA ~65º. The location of each of these ghosts is dependent on field position, generally extending radially outward from their field-center position (which may be offset from the star center) in the direction away from field center. For the F275W (top) image the filter ghost level is <0.1% and is not obvious (Brown, 2007). Noticeably absent from these images are the flares and rings of dots detected in deep ground test point source images; confirming our suggestion that they were artifacts of the CASTLE stimulus (Hartig, 2008a).

For each of the composite images, the EE and azimuthally-averaged (AA) PSF (fractional flux per pixel) were computed as a function of radius, from ~ 1px to 6 arcsec, and plotted in Figure 4, along with the EE specification values in the core and wings at 250 and 633 nm, which are shown as linked crosses. The scatter at small radius is due to the sensitivity to PSF centration relative to the pixel boundaries. The wing EE specs are clearly exceeded, in all cases, and the small decrement from the effective wavelength (~272 nm) of the F275W PSF to that expected at 250 nm does not change this result.

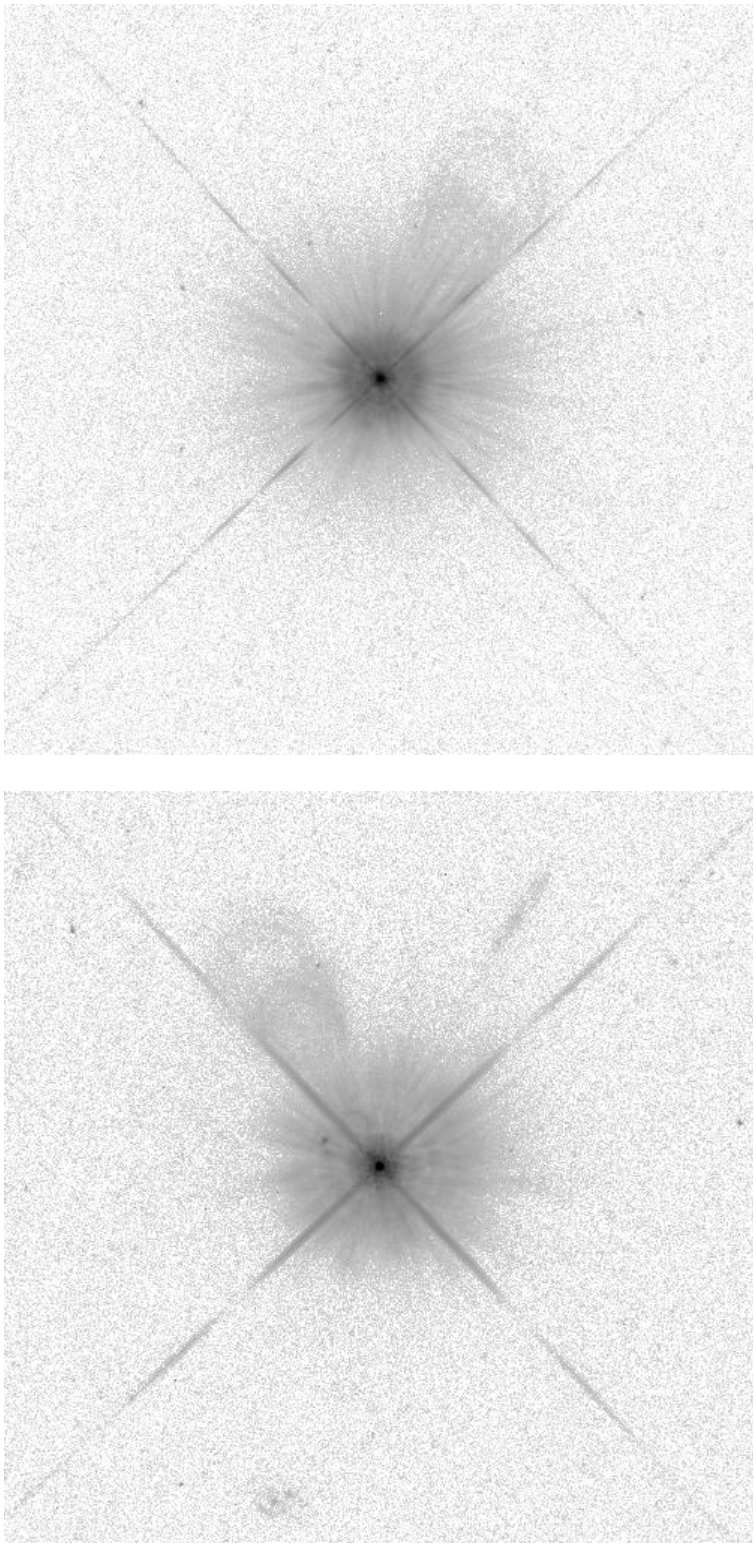

Figure 3 . DeepPSF images from Program 11438 for filter F275W (top) and F625W (bottom) displayed with a 6 dex log stretch. The top image is in the B amp (UR) corner of the UVIS field while the bottom image is in the A amp (UL) corner. Each image subtends ~20 arcsec on a side and is not distortion-corrected. Low-level ghosts due to the detector windows are evident, as well as some field objects.

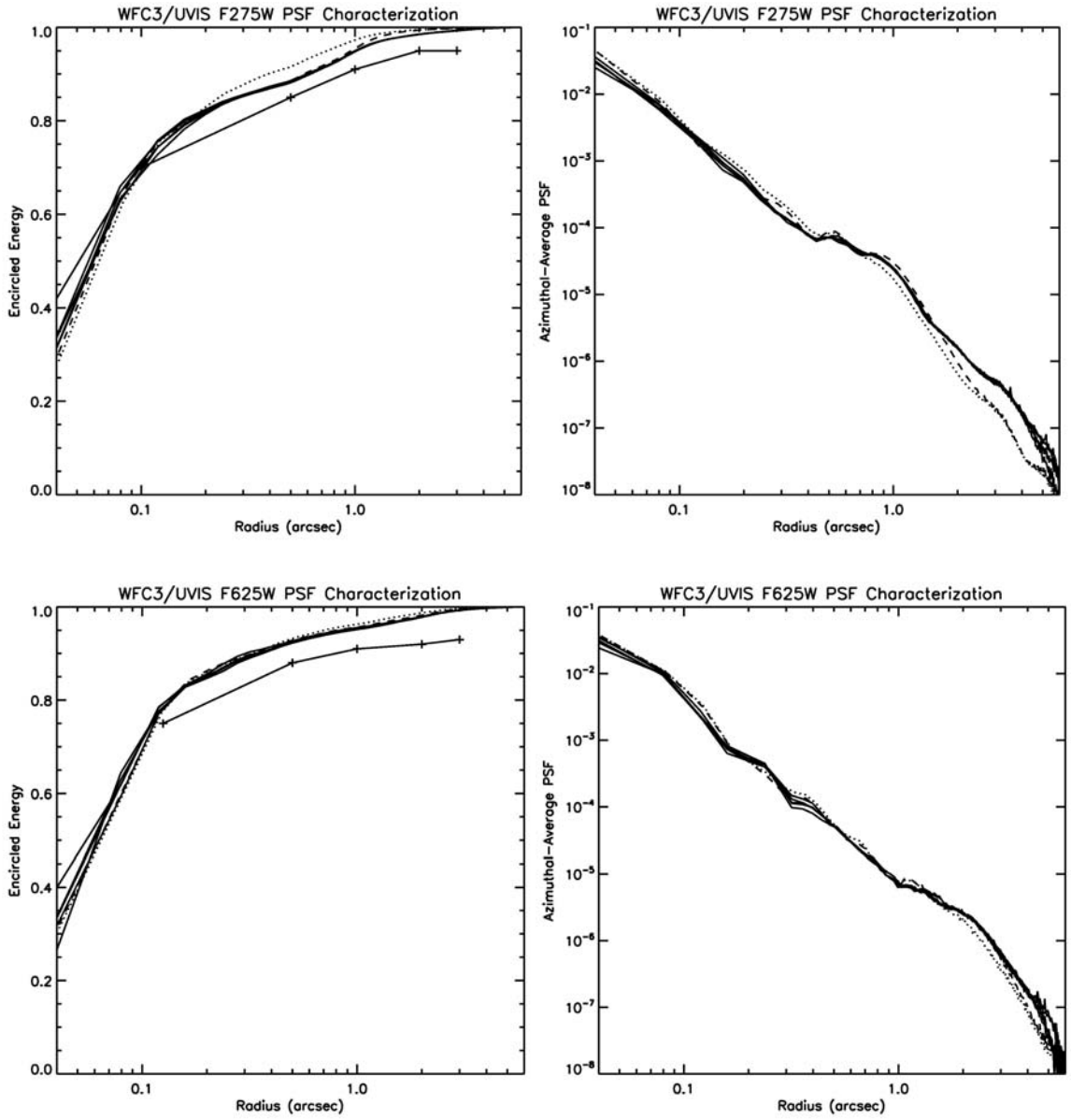

Figure 4 . Encircled energy and azimuthally-averaged PSF (fractional flux per pixel) vs. radius for each of the five deep PSFs from Proposal 11438 for filter F275W (top) and F625W (bottom). Revised model shown as dashed lines, original model as dotted. EE specs are connected crosses.

Modeling

In order to extrapolate these observed data to other wavelengths, we begin with modeling the measured PSFs using straightforward calculations, including only an assessment of the low order WFE from design and alignment residuals, the OTA pupil geometry, the OTA mirror mid-frequency optical path difference (OPD) maps, and a reasonable estimate of the detector-induced blur, due mostly to charge diffusion. The latter is approximated by convolving the PSF with a Gaussian kernel, the width of which is wavelength dependent (Hartig 2008a). The resultant PSFs were then evaluated with the same tools as the measured PSFs and results shown as dotted lines in Figure 4. The agreement between measurement and model is reasonable, from radii of 40 mas (1px) to 5 arcsec, but the

model somewhat over-predicts the EE for F275W beyond ~ 0.2 arcsec. A similar effect of about the same magnitude and radius range is also seen in analogous measurement/model comparisons of the ACS HRC at NUV wavelengths. We conjecture that this is due to spatial frequency limitations of the OTA mirror maps. By filtering the primary mirror OPD map in the frequency domain, emphasizing the power at higher frequencies, we are able to improve the model fit in the 0.2 – 1.2 arcsec radius range. However, this technique cannot add sufficient power at high enough frequencies to improve the fits at larger radii. The unmodeled detector window ghosts also contribute more significantly to the AA PSF at larger radii. The filtered-map model results are shown as dashed lines in Figure 4.

Using this revised model, we can compute PSFs and measure their relevant characteristics to estimate performance over the full wavelength range of the UVIS channel. Results are listed in tables 5-8.

Table 5. On-orbit PSF Model Encircled Energy vs. Radius Estimates

λ(μ):	0.2	0.3	0.4	0.5	0.6	0.7	0.8	0.9	1.0	1.1
0.10	0.660	0.739	0.754	0.745	0.720	0.687	0.650	0.623	0.612	0.605
0.15	0.717	0.793	0.823	0.834	0.832	0.823	0.807	0.778	0.742	0.699
0.20	0.752	0.822	0.845	0.859	0.859	0.857	0.853	0.847	0.844	0.829
0.25	0.781	0.844	0.864	0.875	0.877	0.874	0.870	0.867	0.868	0.864
0.30	0.802	0.858	0.880	0.888	0.890	0.889	0.883	0.879	0.879	0.876
0.40	0.831	0.880	0.899	0.911	0.910	0.907	0.906	0.904	0.900	0.894
0.50	0.861	0.894	0.912	0.923	0.925	0.923	0.918	0.915	0.918	0.917
0.60	0.884	0.906	0.922	0.932	0.934	0.933	0.931	0.927	0.927	0.923
0.80	0.936	0.928	0.936	0.944	0.947	0.946	0.945	0.942	0.944	0.942
1.00	0.967	0.946	0.948	0.954	0.955	0.955	0.955	0.952	0.955	0.952
1.50	0.989	0.984	0.973	0.970	0.970	0.969	0.967	0.966	0.970	0.968
2.00	0.994	0.992	0.989	0.985	0.980	0.977	0.976	0.975	0.978	0.976

Table 6. On-orbit PSF Model Ensquared Energy Estimates

λ(μ):	0.2	0.3	0.4	0.5	0.6	0.7	0.8	0.9	1.0	1.1
1	0.126	0.165	0.184	0.188	0.180	0.166	0.149	0.132	0.117	0.103
2	0.354	0.412	0.431	0.437	0.434	0.423	0.405	0.380	0.352	0.322
3	0.546	0.610	0.613	0.600	0.578	0.563	0.553	0.543	0.531	0.510
5	0.681	0.760	0.784	0.783	0.767	0.738	0.699	0.662	0.638	0.624
7	0.725	0.800	0.827	0.839	0.839	0.832	0.821	0.802	0.775	0.737
9	0.757	0.826	0.849	0.861	0.861	0.860	0.856	0.851	0.849	0.838
11	0.782	0.845	0.866	0.876	0.878	0.874	0.870	0.869	0.869	0.864
13	0.801	0.858	0.880	0.889	0.890	0.888	0.883	0.878	0.880	0.877
15	0.816	0.868	0.891	0.900	0.900	0.899	0.895	0.889	0.888	0.884
17	0.830	0.879	0.898	0.909	0.909	0.907	0.905	0.900	0.898	0.892
19	0.843	0.887	0.905	0.916	0.916	0.914	0.911	0.909	0.909	0.902
21	0.857	0.893	0.910	0.922	0.923	0.920	0.917	0.914	0.917	0.911
23	0.868	0.899	0.916	0.926	0.928	0.926	0.923	0.919	0.921	0.919
25	0.879	0.905	0.920	0.930	0.932	0.931	0.928	0.924	0.926	0.923
51	0.978	0.964	0.957	0.962	0.962	0.961	0.961	0.959	0.962	0.960
101	0.996	0.994	0.992	0.992	0.987	0.984	0.982	0.980	0.983	0.981

Table 7. On-orbit PSF Model Sharpness Estimates

λ(μ):	0.2	0.3	0.4	0.5	0.6	0.7	0.8	0.9	1.0	1.1
Ctr'd	0.041	0.056	0.061	0.061	0.058	0.053	0.048	0.043	0.039	0.035
Cornr	0.040	0.051	0.055	0.055	0.053	0.050	0.047	0.042	0.038	0.034

Table 8. On-orbit PSF Model FWHM Estimates

λ(μ):	0.2	0.3	0.4	0.5	0.6	0.7	0.8	0.9	1.0	1.1
px	2.069	1.870	1.738	1.675	1.681	1.746	1.844	1.960	2.091	2.236
arcsec	0.083	0.075	0.070	0.067	0.067	0.070	0.074	0.078	0.084	0.089

Conclusion

We conclude that the on-orbit optical performance of the WFC3 UVIS channel is generally excellent, as predicted from ground test and analysis. Table 9 lists the relevant CEI specs (requirements and goals) which we are able to verify with the data described herein, along with their pre-flight predictions and the directly measured or derived on-orbit values. The measured core EE values require small corrections, derived from the model, to compare to the monochromatic specifications; these amount to factors 0.975 and 0.996 to be applied to the F275W and F621M measurements, respectively. All EE requirements are satisfied, and the goal for the PSF core EE at 633 nm is nearly achieved. The predictions are generally close to the measurements, but, as described above, the modeling required to extrapolate ground performance to that with the OTA is uncertain, and the mirror maps required modification to better match the observed PSFs, especially in the near wings of UV PSFs.

Table 9. On-orbit UVIS Image Quality Spec Conformance

λ(μ)	Diam (")	Req	Goal	Predict	Meas
0.25	0.20	0.70	0.80	0.71	0.72
	1.00	0.85		0.91	0.88
	2.00	0.91		0.98	0.95
	4.00	0.95		0.99	0.98
	6.00	0.95		0.99	0.99
0.633	0.25	0.75	0.80	0.80	0.79
	1.00	0.88		0.94	0.92
	2.00	0.91		0.96	0.95
	4.00	0.92		0.98	0.98
	6.00	0.93		0.99	0.99

We have produced an optical model that produces PSFs in general agreement with the observed field-averaged UVIS PSF; this model may be used to predict optical performance parameters for purposes of observation planning. A more detailed model, including variation over the field, awaits further analyses.

Acknowledgements

The author is grateful to Linda Dressel for assistance in the instrument optical alignment and for critical reading of this report.

References

Brown, T. “UVIS Channel Filter Ghosts After Filter Replacement”, STScI ISR WFC3-2007-09, 2007.

Hartig, G.F. and Baggett, S. “Preliminary WFC3 UVIS PSF Evaluation”, STScI ISR WFC3-2004-08, 2004.

Hartig, G.F. “WFC3 UVIS PSF Evaluation in Thermal-Vacuum Test #3”, STScI ISR WFC3-2008-40, 2008a

Hartig, G.F. “WFC3 Optical Wavefront Error Characterization in Thermal-Vacuum Test #3”, STScI ISR WFC3-2008-31, 2008b.

Hartig, G.F. “WFC3 SMOV Proposals 11437/9: IR On-orbit PSF Evaluation”, STScI ISR WFC3-2009-37, 2009